J Adv Ceram

Research Article

Concurrent surface and bulk modification of ceria-based cathodic catalyst for CO_2 reduction in solid oxide electrolysis cell under strong polarization conditions

Yongjian Chen[1], Ciyuan Deng[1], Wanying Luo[1], Hongming Ye[1], Rui Yang[1], Manish Singh[2], Te-Wei Chiu[3,4], Liangdong Fan[1,✉]

Cite this article: Chen Y, Deng C, Luo W, et al. *J Adv Ceram* 2026, **15**(1): 9221219. https://doi.org/10.26599/JAC.2025.9221219

ABSTRACT: High-temperature solid oxide electrolysis cells (SOECs) offer high energy efficiency and environmental compatibility for CO_2 conversion but currently face the critical challenges of phase instability and coke formation, especially under the strong polarization conditions. In this study, redox phase-stable CeO_2 cathode materials were modified by co-doping with Mn and Ni, enabling the *in situ* formation of self-assembled and strongly coupled metal Ni/ceria heterostructures and the modification of bulk properties by increasing redox Ce^{3+} active site numbers, Ni exsolution, oxygen defect concentrations, and electrical properties, which consequently effectively enhanced surface reaction kinetics and electrode series conductivity. The optimized Mn–Ni codoped ceria (CMN) exhibited stable electrochemical performance for nearly 140 h at 750 °C with minimal degradation under mild electrolysis conditions. Under strong polarization (2.0 V) condition, SOECs based on the CMN electrode delivered an impressive current density of 3.05 A·cm^{-2} at 800 °C, accompanied by reliable operational stability over the state-of-the-art Ni-based cermet and widely investigated perovskite oxide cathode catalysts. These findings underscore the synergistic benefits of transition metal codoping and *in situ* heterostructure engineering in enabling high-performance, carbon-tolerant ceria-based electrodes for SOEC operation under both moderate and harsh operating conditions, advancing practical application.

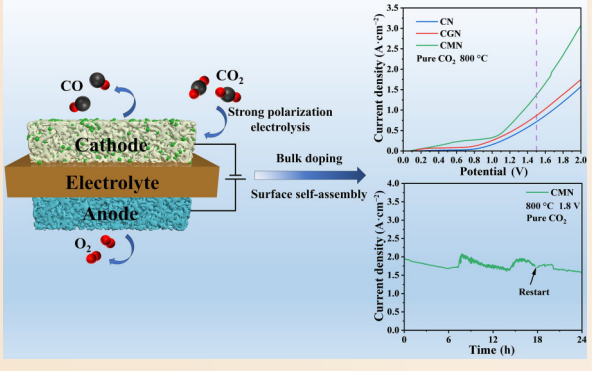

KEYWORDS: solid oxide electrolysis cells (SOECs); CO_2 reduction; self-assembly; strong polarization conditions; ceria (CeO_2)

1 Introduction

With the rapid advancement of modern society, the demand for fossil fuels has continued to increase. However, the excessive reliance on conventional energy sources has led to substantial emissions of greenhouse gases, such as CO_2 and NO_x. Among these, the accumulation of CO_2 is recognized as a major contributor to global warming [1], highlighting the urgency of developing CO_2 capture/utilization/storage and renewable energy technologies [2,3]. In response to these challenges, the conversion of CO_2 into value-added CO and other combustible gases, or its transformation into hydrocarbon fuels via advanced technologies such as the Fischer–Tropsch process, has emerged as promising approaches [4]. In particular, the electrocatalytic reduction of CO_2 offers a highly efficient and cost-effective pathway [4–6]. Among the various electrochemical technologies under investigation, CO_2 electroreduction via solid oxide electrolysis cells (SOECs) has garnered considerable attention [7–9]. This high-temperature electrochemical conversion method not only enables the sustainable storage of intermittent renewable energy in the form of chemical energy but also features high energy efficiency and strong environmental compatibility by mitigating greenhouse gas, enabling the highest technical readiness level among all CO_2 conversion technologies [10–12].

Under SOEC operating conditions, the cathode serves as the site for the carbon dioxide reduction reaction (CO_2RR), while the oxygen evolution reaction occurs at the anode. The electrode electrochemical processes can be described by Reactions (1) and (2) [13–16]:

[1] Shenzhen Key Laboratory of New Lithium-ion Batteries and Mesoporous Materials, Department of New Energy Science and Technology, College of Chemistry and Environmental Engineering, Shenzhen University, Shenzhen 518060, China. [2] Department of Metallurgical and Materials Engineering, Indian Institute of Technology Patna, Bihta 801106, India. [3] Department of Materials and Mineral Resources Engineering, "National" Taipei University of Technology, Taipei 106, Taiwan, China. [4] Institute of Materials Science and Engineering, "National" Taipei University of Technology, Taipei 106, Taiwan, China.

✉ Corresponding author. E-mail: fanld@szu.edu.cn

Received: September 24, 2025; Revised: November 5, 2025; Accepted: November 25, 2025

$$CO_2 + 2e^- + V_O^{\cdot\cdot} = CO + O_O^\times \quad (1)$$

$$O_O^\times = \frac{1}{2}O_2 + 2e^- + V_O^{\cdot\cdot} \quad (2)$$

In this context, $V_O^{\cdot\cdot}$ denotes the number of oxygen vacancies on the electrode surface, whereas $O_O^\times$ refers to the number of lattice oxygen ions occupying these vacancies. Nonetheless, the widespread deployment of SOEC technology is currently hindered by the limited operational stability, which is related mainly to the insufficient activity and instability of the cathodic catalysts, as they meet severe CO_2 reduction conditions, such as high temperatures, redox cycles, CO_2 corrosion, and high electrical reduction potentials [16]. Moreover, owing to its linear geometry and the relatively high bond dissociation energy of the C=O bond (~750 kJ/mol), the rate-determining step of the CO_2RR process in SOECs typically occurs at the cathode side [17,18]. Consequently, research and development efforts prioritizes the exploration of active and reliable cathode materials for SOECs [1].

In the SOEC operating mode, the cathodic CO_2RR can be broadly divided into the following five elementary steps [1,16,19]:

1) CO_2 gas ($CO_{2,gas}$) is adsorbed onto the surface of the cathode catalyst, simultaneously interacting with an $V_O^{\cdot\cdot}$ and one electron to form surface-adsorbed CO_2 species ($CO_{2,ad}^{\cdot}$), as shown in Reaction (3):

$$CO_{2,gas} + e^- + V_O^{\cdot\cdot} = CO_{2,ad}^{\cdot} \quad (3)$$

2) $CO_{2,ad}^{\cdot}$ subsequently reacts with a nearby $O_O^\times$ and receives one electron to form a surface bidentate carbonate species ($CO_{3,ad}$), as shown in Reaction (4):

$$CO_{2,ad}^{\cdot} + O_O^\times + e^- = CO_{3,ad} \quad (4)$$

3) $CO_{3,ad}$ dissociates into adsorbed CO (CO_{ad}) and two lattice oxygens ($O_O^\times$), as shown in Reaction (5):

$$CO_{3,ad} = CO_{ad} + 2O_O^\times \quad (5)$$

4) One $O_O^\times$ dissociates to generate an O^{2-} (which subsequently migrates toward the anode) and an $V_O^{\cdot\cdot}$, as shown in Reaction (6):

$$O_O^\times = O^{2-} + V_O^{\cdot\cdot} \quad (6)$$

5) Finally, the CO_{ad} desorbs and is released as gaseous CO (CO_{gas}), as shown in Reaction (7):

$$CO_{ad} = CO_{gas} \quad (7)$$

To achieve efficient CO_2 reduction, cathode catalysts must first exhibit moderate CO_2 adsorption, high activation, and low CO desorption capacity. Traditional Ni-based cermet electrodes, such as Ni–YSZ, have excellent catalytic activity but suffer from carbon deposition, nickel particle agglomeration, and oxidation issues, all of which compromise long-term stability [20–23]. Perovskite oxides such as well-studied $Sr_2Fe_{1.5}Mo_{0.5}O_{6-\delta}$ [24,25], $(La,Sr)FeO_{3-\delta}$ [26], and $La_{0.75}Sr_{0.25}Cr_{0.5}Mn_{0.5}O_{3-\delta}$ [16], which have mixed electronic and ionic conductivities [27,28], display excellent carbon deposition resistance. However, they suffer from low catalytic activity compared with the Ni-based cermet electrode and insufficient electrochemical phase structural stability, especially under strong polarization conditions [18,29]. Various strategies, such as mechanical mixing with highly ionic conductive electrolytes [30], impregnation with active nanoparticles [19], cation/anion site doping [31,32], metal exsolution [32,33], and *in situ* self-assembly of heterostructures [18,34,35], help improve the CO_2RR rate, but performance degradation under strong polarization and high current conditions remains a challenge [18,29]. Notably, versatile perovskite oxides have been proposed and developed for the CO_2RR in SOECs, but most durability testings were performed under mild operating conditions, i.e., the current density applied is generally lower than 1 A·cm^{-2}, and/or the applied cell voltage is lower than 1.5 V, severely inhibiting the potential applicability of SOEC technology [32,36]. This is caused mainly by the detrimental A-site segregation and phase transformation, even decomposition, of perovskite oxide under excessively high voltages [36,37].

Fortunately, as promising alternatives, fluorite-type ceria (CeO_2) materials offer advantages in terms of structural stability, in addition to adjustable oxygen vacancies and redox flexibility between Ce^{3+} and Ce^{4+} [38–41]. These features not only enhance catalytic activity but also suppress carbon deposition by promoting the formation of gaseous CO species and facilitating the reverse Boudouard reaction ($C + CO_2 \rightarrow 2CO$) [42,43], shedding light on the cost-effective and ideal structural stability under strong polarization–high current working conditions compared with those of Ni-based cermet and perovskite oxide counterparts [44]. However, the intrinsic limitations of pure CeO_2, namely, its low electronic conductivity and insufficient Ce^{3+} concentration under typical operational conditions (its doped form is used as a functional electrolyte for solid oxide cells), still restrict its electrochemical performance, underscoring the need for further material optimization. In previous studies, the main focus has been on increasing the number of active sites by doping with transition metals, such as Ni [45], Fe [39,46], and Co [46], and those metals subsequently exsolve and are finely dispersed at the surface of ceria, forming a socketed nanometal/ceria heterostructure with an active interface, which indeed improves the catalytic activity. However, the overall electrochemical performance is still limited because of the low density of active sites and insufficient bulk electronic conductivity. A high content of transition metal doping and exsolution is not favored, as bulk transitional metals may result in detrimental coking formation. Typical rare-earth elements such as Gd [47] and Sm [48] mainly contribute to increased oxygen vacancy concentrations and ionic conductivity; their influence on bulk ceria properties is limited. Since the Ce^{3+} content in ceria-based electrodes is highly related to the electronic conductivity and electrode active site, methods that increase its concentration under typical CO_2 reduction conditions should be developed [38,49]. Furthermore, when multiple dopants are introduced simultaneously, synergistic effects may arise between the different substitutions. These interactions can optimize defect structures, increase the number of surface active sites, and further enhance charge transport, ultimately resulting in superior CO_2RR performance [45,50]. These multifaceted improvements highlight the potential of codoping strategies in advancing ceria-based materials for highly efficient SOECs.

This study is dedicated to enhancing the catalytic performance of ceria-based materials through improving both their electronic and ionic conductivity, as well as their catalytic activity through doping with Mn and Ni, coupled with the *in situ* exsolution of metallic Ni at elevated temperature of 800 °C (Fig. 1). Notably, the rationale for Mn substitution is slightly different from that of Sm/Gd doping: Although its doping shares the same principle by creating more oxygen vacancies and increasing the Ce^{3+} concentration, its valence state under atmospheric conditions and the formation of redox-stable oxide phase improve the parent oxides' electronic conductivity and help maintain electrode microstructure stability, which are extremely important for ceria-based electrocatalysts to reduce the series resistance originating from the electrode. We aim not only to optimize the physicochemical properties of the ceria-based electrode material

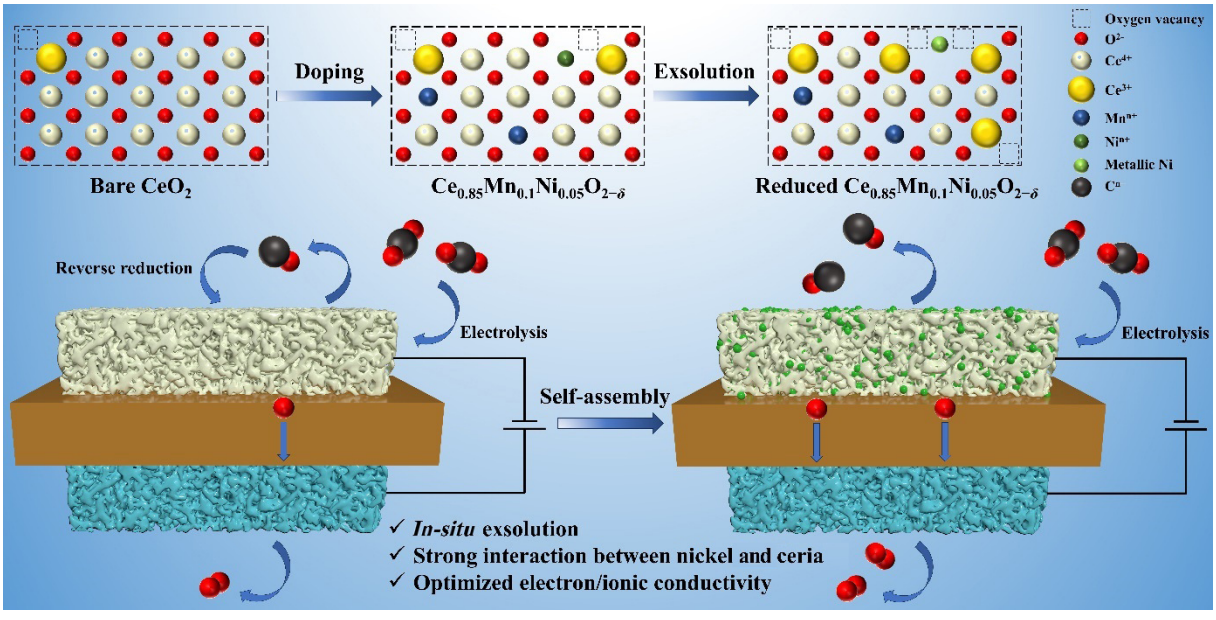

Fig. 1 Schematic illustration of synergetic strategy of codoping and *in situ* self-assembly of a ceria-based cathode for CO_2 reduction.

but also to elucidate the underlying interaction mechanisms on the modified oxide surface, which is characterized by the presence of multivalent Mn ions, exsolved Ni nanoparticles, and the CO_2 reaction environment. Moreover, its electrocatalytic performance and durability under rarely touched strong polarization conditions have been investigated and discussed, considering that a high applied operating voltage not only reduces cathodic ceria, resulting in a high concentration of Ce^{3+} (or a high Ce^{3+}/Ce^{4+} ratio) but also promotes further exsolution of Ni nanoparticles compared with a high-temperature reducing atmosphere, resulting in the formation of a fine dispersed and extended Ni–ceria active interface, which consequently enhance electrocatalytic activity for CO_2 reduction. A comprehensive investigation of these interactions will provide deeper insight into how such bulk/surface modifications and proper choices of operational conditions influence electrode performance and stability during the CO_2RR in SOECs.

2 Experimental methods

2.1 Materials synthesis

CeO_2, $Ce_{0.95}Ni_{0.05}O_{2-\delta}$ (CN), $Ce_{0.9}Mn_{0.10}O_{2-\delta}$ (CM), $Ce_{0.85}Gd_{0.10}Ni_{0.05}O_{2-\delta}$ (CGN), and $Ce_{0.85}Mn_{0.10}Ni_{0.05}O_{2-\delta}$ (CMN) powders were synthesized via the sol–gel method. $Ce(NO_3)_3{\cdot}6H_2O$ (99.99%, Macklin), $Gd(NO_3)_3{\cdot}6H_2O$ (99.99%, Macklin), $Mn(NO_3)_2{\cdot}4H_2O$ (99%, Aladdin), and $Ni(NO_3)_2{\cdot}6H_2O$ (99.99%, Macklin) were dissolved in deionized water at stoichiometric ratios, and the precursor solution was stirred at 80 °C until it became a transparent solution. Then, citric acid monohydrate (99.5%, Aladdin) and ethylene-diamine-tetra-acetic acid (EDTA; 99.5%, Aladdin) were added successively to the above solution according to the molar ratio of *n*(cations) : *n*(citric acid) : *n*(EDTA) = 1 : 2 : 1, followed by an ammonia solution (25%–28%, Aladdin) to adjust the pH of the solution to 7–8 for absolute dissolution of the metal salts. The precursor solution was dried at 200 °C for 5 h, and then, the dried powders were subjected to heat treatment at 1000 °C for 5 h at a heating rate of 5 °C·min^{-1} to obtain well-crystallized fuel electrode powders.

The anode material $La_{0.6}Sr_{0.4}Co_{0.2}Fe_{0.8}O_{3-\delta}$ (LSCF) powder was also synthesized via the sol–gel method, except that the added raw material was changed to $La(NO_3)_2{\cdot}6H_2O$ (99%, Macklin), $Sr(NO_3)_2$ (≥ 99.0%, Aladdin), $Fe(NO_3)_2$ (98.5%, Macklin), and $Co(NO_3)_2{\cdot}6H_2O$ (99%, Aladdin), and the precursor was calcined at 900 °C for 5 h. The other procedures were the same as those for the ceria-based cathode material. Finally, the synthesized LSCF powder and commercial $Ce_{0.8}Gd_{0.2}O_{2-\delta}$ (GDC; SOFCMAN, China) were mechanically mixed by ball-milling at a weight ratio of 5 : 5 for 24 h in a planetary mill (YXQM-1L, MITR) using ethanol as the solvent at a rotation speed of 200 r/min to obtain the LSCF–GDC composite anode material. The electrolyte $La_{0.8}Sr_{0.2}Ga_{0.8}Mg_{0.2}O_{3-\delta}$ (LSGM) powder was purchased from Wuxi City Kaistar Electro–Optic Materials Co., Ltd.

2.2 Cell fabrication

First, 0.2 g of LSGM powder was dry pressed and sintered at 1450 °C for 6 h at a heating rate of 2 °C·min^{-1} below 1000 °C, and a heating rate of 1 °C·min^{-1} from 1000 to 1450 °C to obtain a dense sample, which was further polished to a thickness of approximately 200 μm. The GDC was ground with terpineol containing 6 wt% ethyl cellulose at a weight ratio of 2 : 3 for 1 h to prepare the buffer layer slurry. Subsequently, it was coated onto one side of the LSGM electrolyte by spin-coating on a vacuum adsorption spin coater. Finally, the GDC buffer layer was obtained by sintering in air at 1400 °C for 2 h at a heating rate of 2 °C·min^{-1}.

Then, CMN (fuel electrode) or LSCF–GDC (air electrode) powders and terpineol (containing 6 wt% ethyl cellulose) with a 2 : 3 weight ratio were ground for 1 h to obtain the electrode slurry. The CMN slurry was coated on the side with the buffer layer, whereas the LSCF–GDC slurry was coated on the other side without the buffer layer. Single cells were then obtained by sintering in air at 1000 °C for 2 h at a heating rate of 2 °C·min^{-1}. The electrolyte pellet diameter of all the cells was approximately 13.6 mm, with an electrode active area of approximately 0.2826 cm^2. Silver paste (Sino-Platinum Metals Co., Ltd.) was brushed onto the surfaces of both electrodes to serve as the current collector, and a piece of silver wire was attached to each electrode via conductive adhesive to act as the lead wire.

2.3 Materials characterization

The phase structures of the powder samples were detected via an

X-ray diffractometer (XRD; PAN-analytical Empyrean) with Cu Kα radiation at 2θ intervals ranging from 20° to 80°. The crystal structure and lattice parameters of the ceria-based materials were fitted by GSAS refinement. An X-ray photoelectron spectrometer (XPS, K-Alpha+, Thermo Fisher Scientific Inc.) with a monochromatic Al Kα source ($h\nu$ = 1486.6 eV) was used to determine the valence states of the elements on the surface and calculate the oxygen vacancies at high temperatures. A field emission scanning electron microscope (FE-SEM; JSM-7800F & TEAM Octane Plus, JEOL) was used to characterize the ceria-based fuel electrode morphology and the cross-sectional microstructure of the cell. Thermogravimetric analysis (TGA) was performed via a simultaneous thermal analyzer (TGA/DSC 3+, Mettler) to evaluate the oxygen vacancy concentration of each ceria-based material. Prior to testing, the samples were held at 200 °C for 1 h to remove moisture and then heated to 850 °C at a rate of 10 °C·min^{-1} in air. CO_2 temperature-programmed desorption (CO_2-TPD) was employed using a catalyst analyzer (BELCAT-A, Microtrac) to investigate the CO_2 adsorption capacity of the ceria-based materials. Additionally, an electron paramagnetic resonance (EPR) spectrometer (A300-10/12, Bruker) was used under ambient air conditions at room temperature to further quantify the oxygen vacancy concentration. A Raman spectrometer (17008200, Renishaw) was used on the surface of the cell's cathode material before and after the long-term stability test to determine whether carbon deposition occurred.

2.4 Electrochemical tests

Single cells were sealed on the top of a ceramic alumina tube using a ceramic sealant (Ceramabond 552), with the cathode and anode exposed to pure CO_2 and ambient air atmospheres, respectively. The flow rate of pure CO_2 was 50 mL·min^{-1}. The electrochemical performance was evaluated by an electrochemical workstation (VersaSTAT 4, Ametek) from the open-circuit voltage (OCV) to 1.6 or 2.0 V at a scan rate of 10 mV·s^{-1}. The short-term CO_2RR test was performed at constant voltages of 1.2, 1.3, 1.4, and 1.5 V, each of which was stabilized for 20 min at 800 °C. The long-term stability under mild conditions was tested at a constant voltage of 1.1 V at 750 °C. Electrochemical impedance spectroscopy (EIS) measurements were acquired in the frequency range of 10^5–0.1 Hz with an AC amplitude of 20 mV. The distribution of relaxation time (DRT) analysis was studied via DRT tools via MATLAB software with a regularization parameter of 10^{-3} [50,51]. Under strong polarization test conditions, the terminal voltage of the *I*–*V* curves and short-term CO_2RR tests was increased to 1.4–2.0 V. The short-term stability test was conducted at 800 °C under a constant voltage of 1.8 V. The other conditions were consistent with those of the conventional voltage tests.

3 Results and discussion

3.1 Materials phase structure, morphology, and microstructure

As shown in Fig. 2(a), both individual and codoped Mn and Ni were successfully doped within the ceria-based material system after heat treatment in air, with no detectable impurity phase peaks, indicating the formation of a single-phase solid solution. Rietveld refinement of the XRD data reveals that the unit cell volume of the ceria-based materials decreases with increasing metal doping (Table S1 in the Electronic Supplementary Material (ESM)). This contraction can be attributed to the smaller ionic radii of the transition metal cations (Mn and Ni) than that of Ce, whereby their substitution for Ce leads to a reduction in the cell volume. To observe the phase and microstructure of the reduced sample, a mixed atmosphere of 30% CO and 70% CO_2 was used to simulate the working cathodic conditions for a 2-h reducing treatment at 800 °C. The specific mixing gas composition was determined by Faraday's law of electrolysis, and the theoretical CO production rate of the CMN cathode cell at 800 °C under a polarization voltage of 1.8 V was calculated to be 15.48 mL·min^{-1} (assuming 100% current efficiency using the LSGM electrolyte) [52], which accounted for 30% of the CO in the CO/CO_2 mixing gas (the feed gas flow rate was 50 mL·min^{-1}). The *in situ* exsolution behavior of Ni was therefore observed. After reduction, a distinct diffraction peak at 44.3° appeared in the XRD patterns of the CMN, CN, and CGN samples (Figs. 2(b) and 2(c) and Fig. S1 in the ESM), corresponding to the metallic Ni phase. The rough Rietveld quantitative phase analysis results (Fig. S2 in the ESM) confirmed that the Ni metal content increased from 0.36 wt% in the CN sample to 3.85 wt% in the CMN sample (Table S2 in the ESM), suggesting the positive role of Mn doping in promoting the exsolution of the Ni nanoparticles. SEM images further revealed the formation of uniformly dispersed spherical particles on the reduced sample surface (Figs. 2(d) and 2(e), and Figs. S3 and S4 in the ESM), which was consistent with the XRD results. The particles are mainly 30–50 nm in size, suggesting that the applied reducing conditions effectively controlled the Ni particle size. To further identify the exsolved particles, TEM analysis was performed on the reduced CMN sample (Figs. 2(f) and 2(g)). The measured interplanar spacing of 0.238 nm corresponds to the (111) plane of NiO, which is likely due to the oxidation of metallic Ni nanoparticles upon exposure to air. These particles were found to be partially embedded within the ceria matrix; this is frequently observed for exsolved metals reported in Refs. [6,53,54]. This socketed structure results in strong metal–oxide interactions between Ni and CeO_2. This configuration not only increases the number of catalytically active sites (both on exsolved Ni and its related interface) but also contributes to the structural stability of the exsolved nanoparticles, suggesting promising prospects for their application in CO_2 reduction.

3.2 Material surface chemistry

XPS analysis (Figs. 3(a) and 3(b)) revealed that the physically and chemically adsorbed oxygen contents of the ceria-based materials increased progressively with increasing transition metal doping level, suggesting a corresponding increase in the oxygen vacancy concentration. This enhancement is attributed primarily to the substitution of Ce^{4+} ions in the fluorite lattice by lower-valence transition metal cations. To maintain overall charge neutrality, partial release of lattice oxygen (O^{2-}) occurs, thereby generating oxygen vacancies. As discussed above regarding the electroreduction mechanism of CO_2 molecules on SOEC cathode surfaces, these oxygen vacancies act mainly as preferential adsorption centers for CO_2; the doping of transition metals increases the concentration of oxygen vacancies, thereby increasing the population of CO_2 adsorption sites during electrolysis and consequently enhancing the catalytic activity of ceria-based materials for CO_2 electroreduction [39]. XPS peak fitting analysis of the Ce 3d spectrum is shown in Figs. 3(c) and 3(d); the peak pairs labeled u–v and u1–v1 are attributed to Ce^{3+} species, whereas the remaining peaks correspond to Ce^{4+}. These results indicate that transition metal doping not only increases the concentration of oxygen vacancies but also promotes the partial reduction of Ce^{4+} to Ce^{3+}. In the context of CO_2 electroreduction,

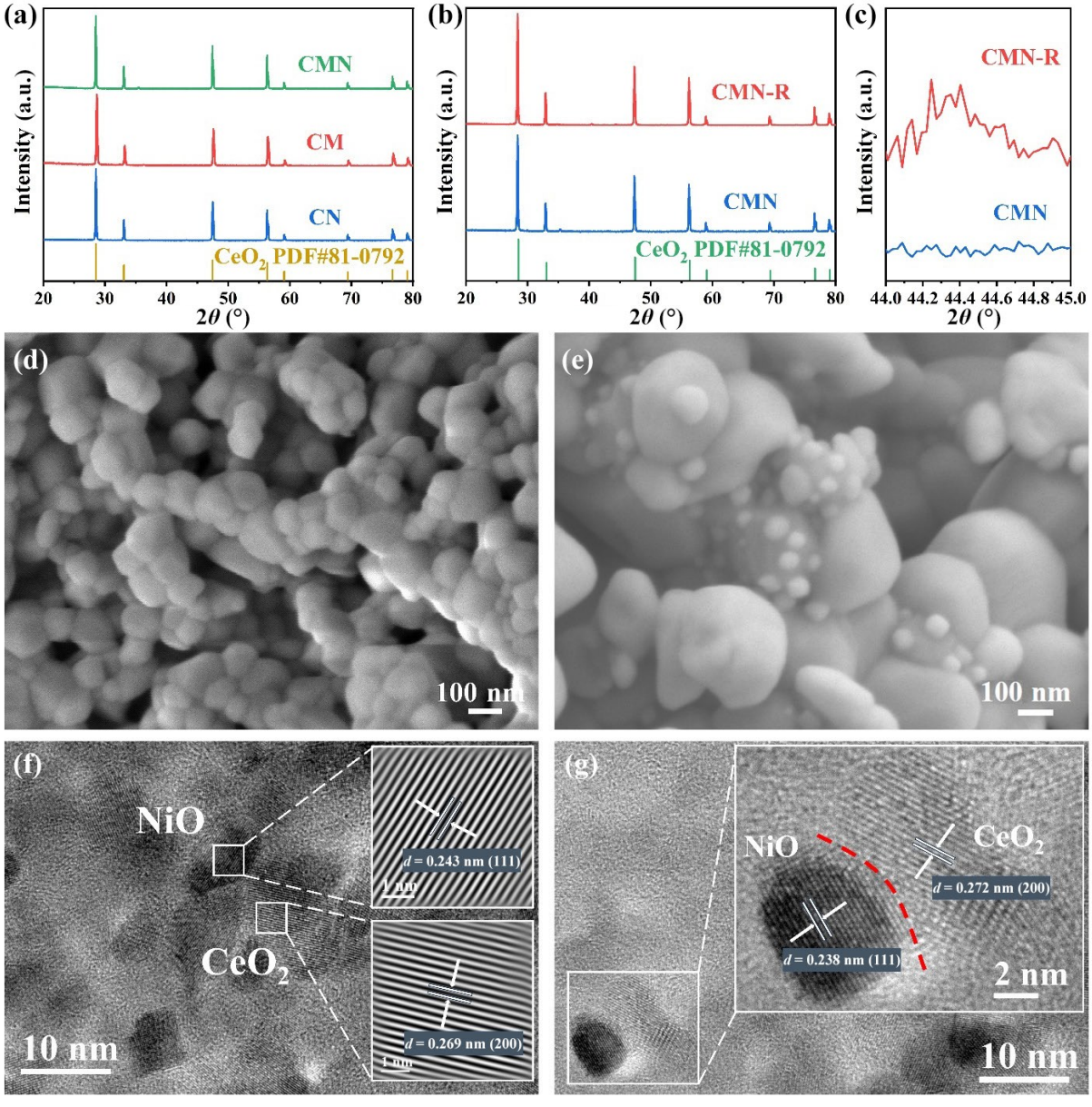

Fig. 2 Phase and microstructure of samples: (a–c) XRD patterns and SEM images of CMN sample (d) before and (e) after reduction; (f, g) TEM images of CMN sample after reduction.

Ce^{3+} plays a crucial role by acting as an electron donor to activate adsorbed CO_2 molecules, thereby facilitating CO_2 activation [38]. Moreover, to maintain overall charge neutrality, the increased number of Ce^{3+} sites further increases the oxygen vacancy concentration. Thus, increasing the Ce^{3+} content in ceria-based materials is advantageous for improving their catalytic performance. The increase in the Ce^{3+} concentration upon Mn and Ni codoping, together with the associated increase in the oxygen defect density, confirms that the dual-metal doping strategy effectively modulates the electronic structure of CeO_2 and enhances its electrocatalytic activity for CO_2 reduction.

Upon being reduced in a 30% CO–70% CO_2 atmosphere, XPS analysis reveals a further increase in the concentration of oxygen vacancies (Figs. S5(a) and S5(c) and Table S3 in the ESM) and Ce^{3+} species (Figs. S5(b) and S5(d) and Table S4 in the ESM) in the ceria-based material. Concurrently, Mn undergoes a valence transition from predominantly +3 to mainly +2, indicating that the doped Mn transition metal is also reduced to a lower oxidation state under a reducing environment (Figs. 3(e) and 3(f) and Table S5 in the ESM), serving as an additional active site for CO_2 reduction. The Ni 2p XPS spectra of the CN and CMN samples before and after reduction are presented in Fig. S6 in the ESM. Compared with the as-prepared samples, both reduced samples exhibit a noticeable shift in the Ni^{2+} signal toward higher binding energies. This positive shift indicates a decrease in the local electron density of the Ni species, which can be attributed to the strengthened electronic interaction between Ni and the surrounding oxide matrix. In particular, the reduced CMN (CMN-R) sample shows a more pronounced shift than the reduced CN (CN-R) sample does, suggesting that the coexistence of Mn dopants and oxygen vacancies facilitates stronger interactions between Ni and the ceria-based lattice. This enhanced interfacial coupling stabilizes the Ni species through charge transfer and chemical bonding with the reducible CeO_2 matrix, which benefits the catalytic activity as well as durability during CO_2 electroreduction. Moreover, the reductive treatment increases the oxygen deficiency in the ceria lattice and modifies the electronic structure of the doped transition metal cations, thereby

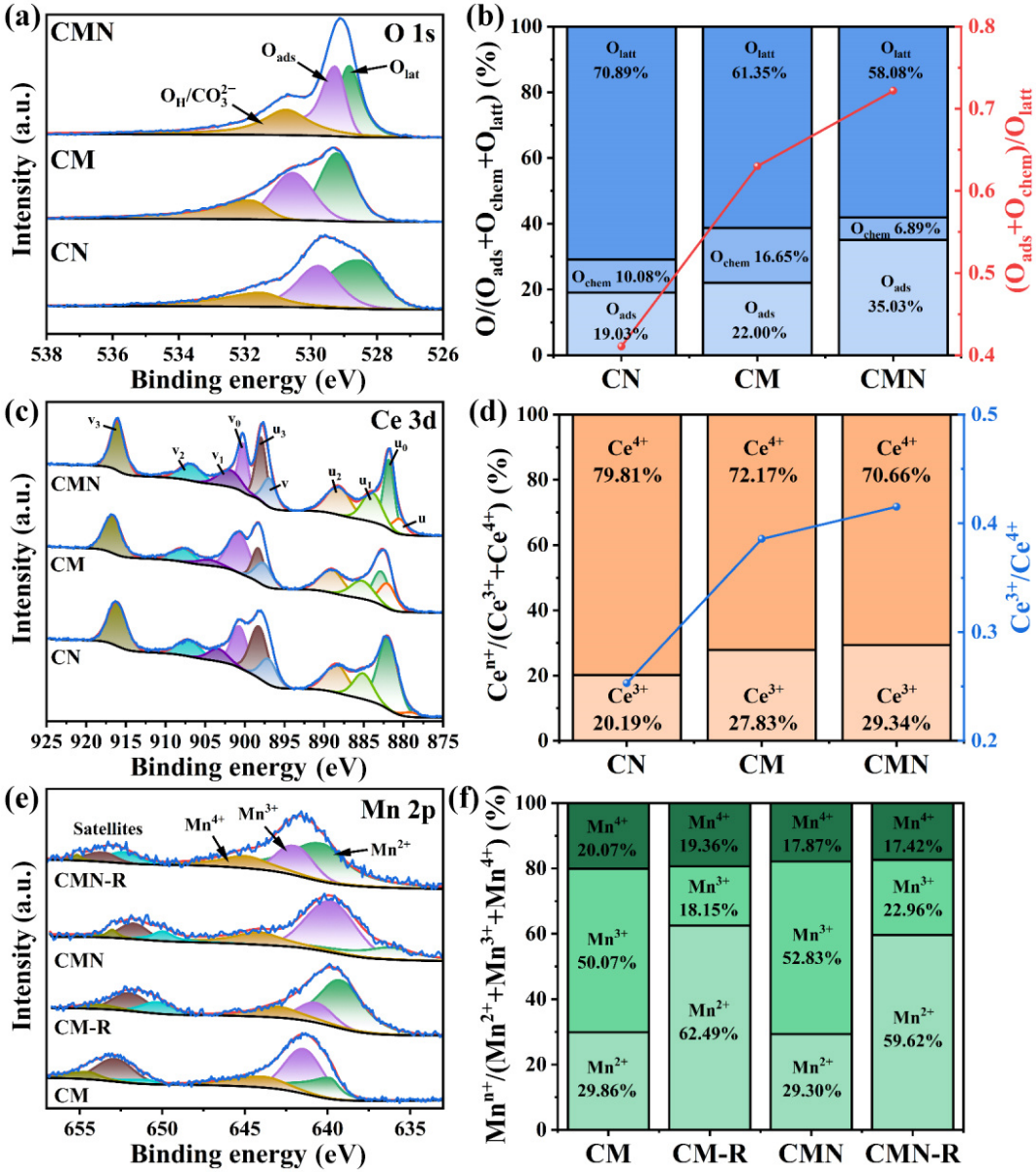

Fig. 3 XPS fitting analysis results of CN, CM, and CMN raw materials: (a) O 1s; (c) Ce 3d; (e) Mn 2p. Contents of (b) O, (d) Ce, and (f) Mn species on the surface of ceria-based materials (O_{chem} refers to chemisorbed oxygen, specifically including O_H and CO_3^{2-}).

promoting the overall reducibility of the material and enhancing its potential for CO_2 electroreduction. Notably, in addition to doping, high temperatures and high electrical cathodic potentials also increase the concentration of Ce^{3+}, which will be detailed later. These findings will also be corroborated by the subsequent Raman spectroscopy presented below.

In Fig. 4(a), in addition to the characteristic Ce^{4+}–O symmetric stretching vibration at approximately 460 cm^{-1}, an additional peak appeared at ~660 cm^{-1} (denoted as the β peak) in the Mn-doped samples (CM and CMN). This β peak is generally attributed to bulk defect sites induced by heteroelement (Mn in this case) doping [38] through the following equation: $MnO \xrightarrow{CeO_2} Mn_{Ce}^{*} + O_O^X + V_O^{\cdot\cdot}$. This suggests that Mn doping significantly increases the bulk concentration of oxygen vacancies. Compared with the CM sample, the codoped CMN material exhibited a slight redshift in the β peak, likely resulting from the combined effects of Mn and Ni codoping, which further increased the oxygen vacancy density. Furthermore, the partial reduction of Ce^{4+} to Ce^{3+}, whose larger ionic radius induces lattice expansion, may also contribute to this redshift in the Raman response [38]. A weak signal at ~505 cm^{-1} (denoted as the α peak) was additionally observed in the CMN sample, which is related to the enhanced oxygen defect structure and elevated Ce^{3+} concentration induced by dual-cation doping. These observations serve to corroborate the XPS findings presented earlier.

A comparison of the TGA curves of the reference samples (CeO_2, CN, CM) and the codoped experimental sample (CMN) clearly reveals that all the materials exhibit similar weight change trends within the temperature range of 300–850 °C (Fig. 4(b)). This consistency reflects their common ceria-based framework, indicating that transition metal doping does not fundamentally alter the intrinsic physicochemical properties of ceria. However, the extent of weight loss follows the order of CMN > CM > CN > CeO_2, with specific losses of 0.246, 0.217, 0.190, and 0.179 wt%, respectively. The greater weight loss observed in the CMN sample suggests a higher concentration of oxygen vacancies, which is positively correlated with the total amount of doped transition metals. EPR characterization further supports this, as the signal

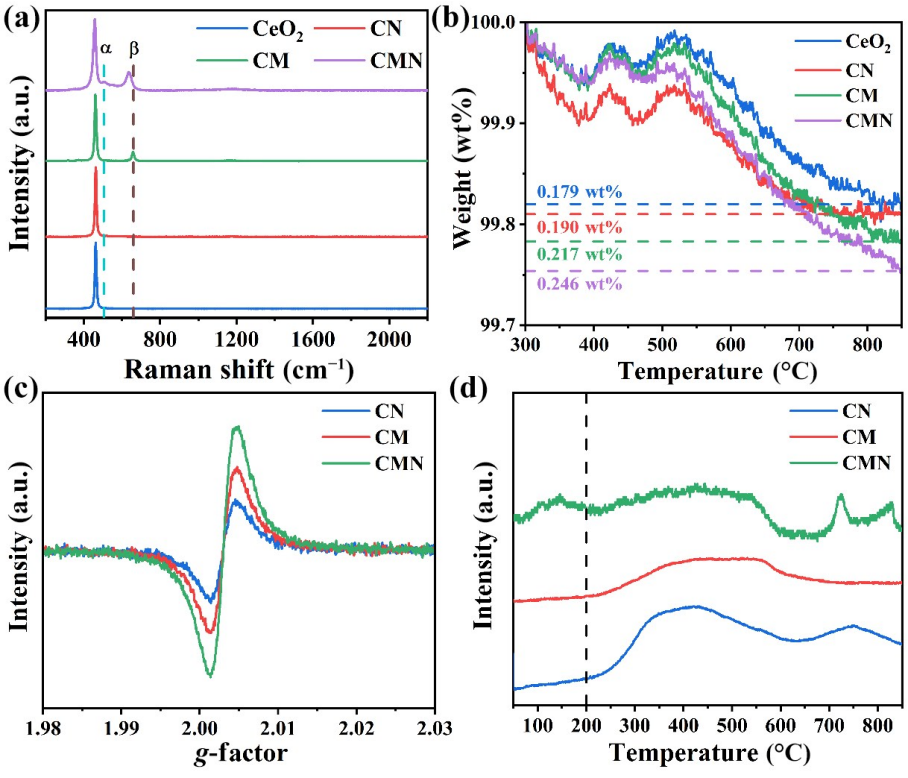

Fig. 4 Bulk and surface chemical properties of ceria-based electrodes: (a) Raman spectra; (b) TGA; (c) EPR; (d) CO_2-TPD (data are offset in *y* for clarity).

intensity increases with increasing doping content, with the CMN sample showing the strongest peak at the *g*-factor of 2.05, confirming that Mn and Ni codoping more effectively induce oxygen vacancies than single doping (Fig. 4(c)). Additionally, CO_2-TPD analysis reveals that the CMN sample presented a stronger CO_2 chemical desorption signal above 200 °C, particularly between 700 and 850 °C (Fig. 4(d)), suggesting that Mn and Ni codoping increase the surface defect density, which strengthens the chemical interaction of the material with CO_2. In summary, the incorporation of low-valence transition metals such as Mn and Ni into ceria-based materials effectively modulates their oxygen defect chemistry and electronic structure. The substitution of Ce^{4+} with lower-valence dopants leads to the generation of abundant oxygen vacancies, which serve as crucial active sites for CO_2 adsorption and activation. Simultaneously, the partial reduction of Ce^{4+} to Ce^{3+} enhances the active site and electron-donating capability of the electrode [38,49], facilitating CO_2 activation and charge transport. These results, combined with the intrinsic Mn and its promoted Ni exsolution effect, will collectively contribute to improving the electrocatalytic performance of doped ceria-based materials in CO_2 reduction from both thermodynamic and kinetic standpoints.

3.3 Electrochemical performance of SOEC under mild conditions

Using LSGM as the electrolyte and an LSCF–GDC composite as the air electrode, along with a GDC buffer layer between the cathode and the electrolyte, SOECs were fabricated with various doped ceria-based materials serving as the CO_2 fuel cathode. As shown in Fig. S7(a) in the ESM, the assembled cell exhibited a well-defined microstructure. The LSGM electrolyte, with a thickness of approximately 225 μm, was dense and compact, effectively preventing direct contact between the reactant gases and the two electrodes. Distinct interfaces can be observed among the cathode, GDC buffer layer, and electrolyte (Fig. S7(b) in the ESM). The buffer layer, with a thickness of approximately 7.5 μm, appeared denser than the cathode due to its higher sintering temperature and was closely bonded to both the electrolyte and the cathode with no discernible interfacial gaps. The ceria-based cathode and LSCF–GDC anode exhibited porous microstructures with thicknesses of approximately 17 and 37 μm, respectively; their grain sizes were uniformly distributed, and most of them were smaller than 1 μm (Figs. S7(c) and S7(d) in the ESM), which contributed to maximizing the specific surface area and promoting electrochemical reaction kinetics.

When operated with pure CO_2, the current densities of the SOECs with the cathode materials CeO_2, CN, CM, and CMN at 800 °C under an applied voltage of 1.5 V were 0.47, 0.62, 1.25, and 1.37 A·cm^{-2}, respectively (Fig. 5(a)). Among them, the SOEC with the CMN cathode exhibits superior CO_2RR performance at 800 °C and 1.5 V, compared to the other reference samples and most of the currently reported works (Figs. S8–S10 and Table S6 in the ESM). The short-term current stability test results, as presented in Fig. S11 in the ESM, demonstrate that all ceria-based cathode materials, regardless of doping, exhibited stable performance under applied voltages of 1.2, 1.3, 1.4, and 1.5 V. Compared with the undoped CeO_2 sample, the doped cathode materials exhibited superior electrolytic current densities and low polarization resistance values under an operating voltage of 1.5 V (Figs. 5(b) and 5(c)). In addition, with the successive incorporation of the transition metals Mn and Ni, the increased number of oxygen vacancies and increased Ce^{3+}/Ni^0 concentration effectively reduce the ohmic and polarization resistances of the ceria-based cathode during CO_2 electroreduction, thereby enhancing the overall electrocatalytic performance (Figs. S12–S16 in the ESM). Since all other cell components remained constant across the different configurations, these results demonstrate that doping ceria with codoped transition metal cations, i.e., Mn and Ni, is an efficient strategy for electrochemical reduction of CO_2.

The long-term current stability of the CMN cell was evaluated

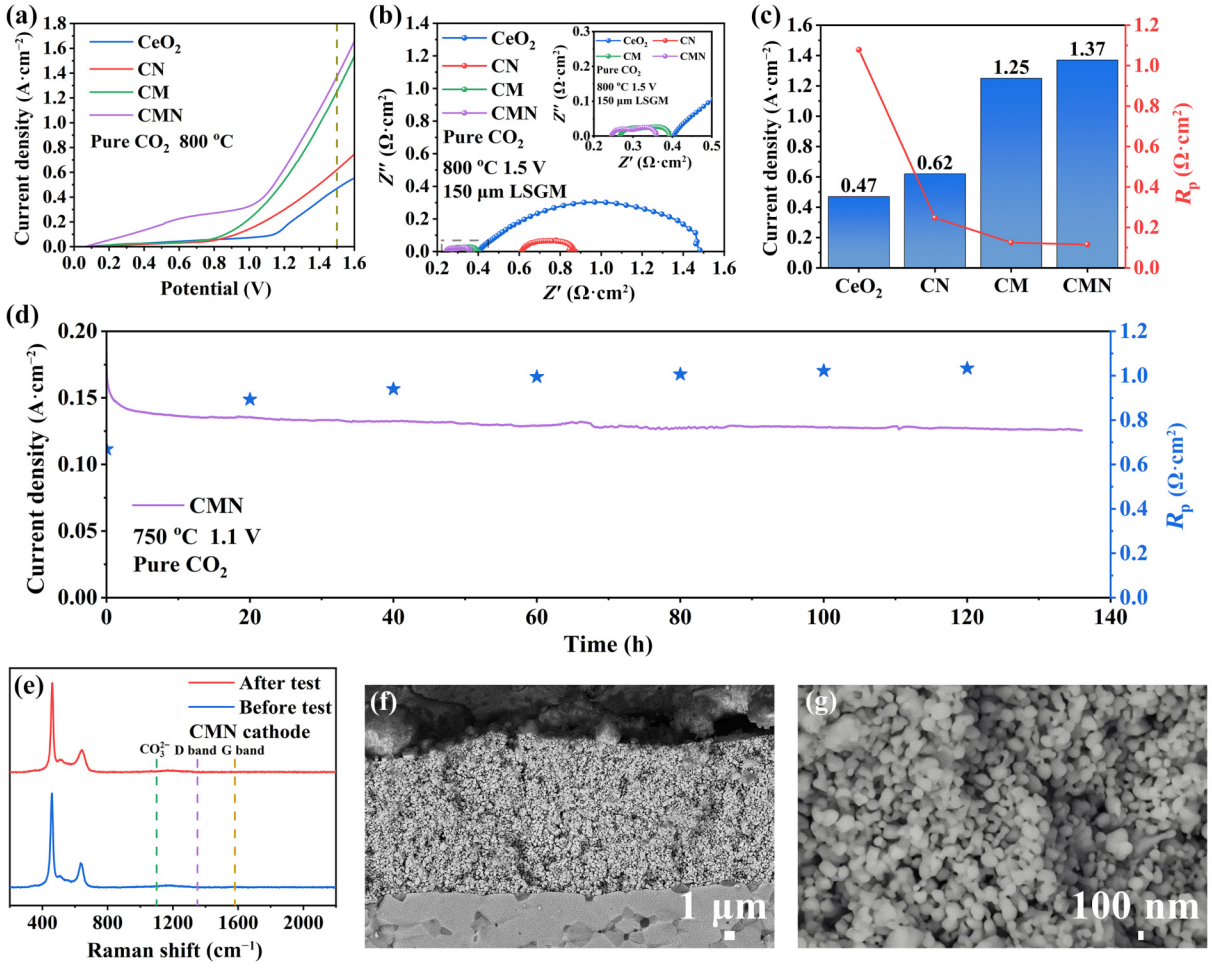

Fig. 5 Electrochemical performance of SOECs with ceria-based cathode materials: (a) *I–V* curves; (b) EIS results; (c) comparison of current densities and polarization resistance at 800 °C and 1.5 V; (d) long-term current stability; (e) Raman spectra and (f, g) SEM images of SOECs with CMN cathode after long-term testing.

under mild operating conditions at 750 °C and a constant cell voltage of 1.1 V, and the results are shown in Fig. 5(d). The CMN cathode maintained stable CO_2 electroreduction performance over a continuous period of approximately 140 h, with a current density degradation rate of only 0.25 mA·cm^{-2}·h^{-1}. *In situ* EIS measurements were conducted at 20-h intervals, although a noticeable increase in the polarization resistance was observed during the first 20 h (Fig. S17 in the ESM), likely because the polarization resistance had not yet reached thermal and electrochemical equilibrium at the beginning of the test. Thereafter, a gradual and steady polarization impedance was recorded over time. The post-test Raman spectroscopy (Fig. 5(e)) revealed no distinct peaks associated with carbonate species or carbon deposition, indicating the absence of carbon accumulation after electrolysis operation. Moreover, compared with the pre-test results, the Raman spectra of the CMN cathode after long-term operation remain nearly unchanged, indicating that the bulk material undergoes no significant structural alterations during prolonged high-temperature electrolysis, thereby demonstrating the redox and electrochemical stability of the modified ceria-based material. Compared with the pre-test state (Fig. S7(c) in the ESM), the cathode shows no significant microstructural changes, with the material particles remaining well dispersed and without obvious agglomeration (Figs. 5(f) and 5(g)). In addition, no evident delamination was observed in the tested cell, indicating considerable structural integrity (Fig. S18 in the ESM). This demonstrates that the modified ceria-based material possesses ideal structural stability under high-temperature electrolysis conditions, which in turn underpins its ability to maintain stable electrochemical performance during the long-term CO_2RR.

3.4 Electrochemical performance of SOEC under strong polarization conditions

Building upon the excellent and reliable CO_2 electroreduction performance demonstrated by ceria-based cathode materials under mild operating conditions and their intrinsic redox crystal structure stability, further evaluation was conducted under strong polarization conditions (above 1.6 V) to assess their applicability in high-current CO_2 electroreduction scenarios, as limited high-temperature electrolysis works have been performed under such harsh conditions due to the high potential for carbon deposition issues at the electrode surface, especially for Ni-based cermet electrodes, and the phase structural instability of commonly used perovskite oxide electrodes [36,55]. Furthermore, the reduction of Ce^{4+} to Ce^{3+} is accelerated under high applied voltages, providing more active sites for CO_2 reduction [38]. To specifically elucidate the role of the multivalent transition metal Mn, a comparative sample (CGN) was also prepared by replacing Mn with Gd, a fixed-valence rare-earth element, while maintaining all other synthesis parameters identical. To ensure a fair comparison, the electrochemical performance of CGN was evaluated exclusively under strong polarization conditions, where the redox activity of multivalent Mn ions (Mn^{4+}/Mn^{3+} and Mn^{3+}/Mn^{2+}) becomes prominent and may also facilitate the Ce^{4+}/Ce^{3+} redox cycle [56,57].

Under milder polarization conditions, such redox-driven enhancement is negligible, whereas the stable valence state of the Gd-doped CGN material provides a limited contribution to electronic conduction; therefore, this material is not included under previous mild operating conditions. Its testing under strong polarization could highlight the distinct effects of the multivalent nature of Mn on the electrochemical behavior of ceria-based cathodes. Electrolysis testing in the voltage range of 1.6–2.0 V revealed that all tested cathodes (CN, CGN, and CMN) exhibited steadily increasing current densities. Notably, the codoped CMN cathode achieved a maximum current density of 3.05 $A{\cdot}cm^{-2}$ at 2.0 V, significantly outperforming both CN (1.56 $A{\cdot}cm^{-2}$) and CGN (1.75 $A{\cdot}cm^{-2}$), as shown in Fig. 6(a)); the cell with the CMN cathode also exhibited superior electrolysis performance compared with those CN and CGN cathodes at both 750 and 850 °C (Figs. S19 and S20 in the ESM); these results directly indicate the promotion role of valence state changeable Mn instead of valence state fixed Gd doping. Notably, the differential conductance (dJ/dV) of all three cathodes increases markedly with increasing applied potential (Fig. 6(b)). This trend indicates a continuous decrease in the effective differential resistance (dV/dJ) under higher bias, reflecting the mitigation of polarization constraints and an enhanced charge transfer and transport process. Among the investigated electrodes, the cell with the CMN cathode exhibits the most pronounced increase in slope, particularly above approximately 1.5 V, where a high-conductance regime is established. This behavior can be rationalized by two synergistic effects: (i) The applied potential enhances the surface catalytic kinetics, thereby lowering the activation barrier for CO_2 adsorption and subsequent electrochemical reduction, and (ii) the strong electric field promotes the partial reduction of Ce^{4+} to Ce^{3+} [38], generating additional oxygen vacancies and defect sites, which facilitate mixed electronic–ionic transport as well as CO_2 adsorption/activation at the electrode surface. The significantly higher slope of CMN than those of CN and CGN under elevated voltages thus confirms its superior ability to exploit the voltage-induced catalytic enhancement and the increased concentration of Ce^{3+}, ultimately resulting in reduced impedance and enhanced electrolysis performance.

EIS results obtained at various voltages and temperatures under pure CO_2 (Figs. S21–S23 in the ESM) further confirmed that CMN exhibited the lowest overall impedance, including both

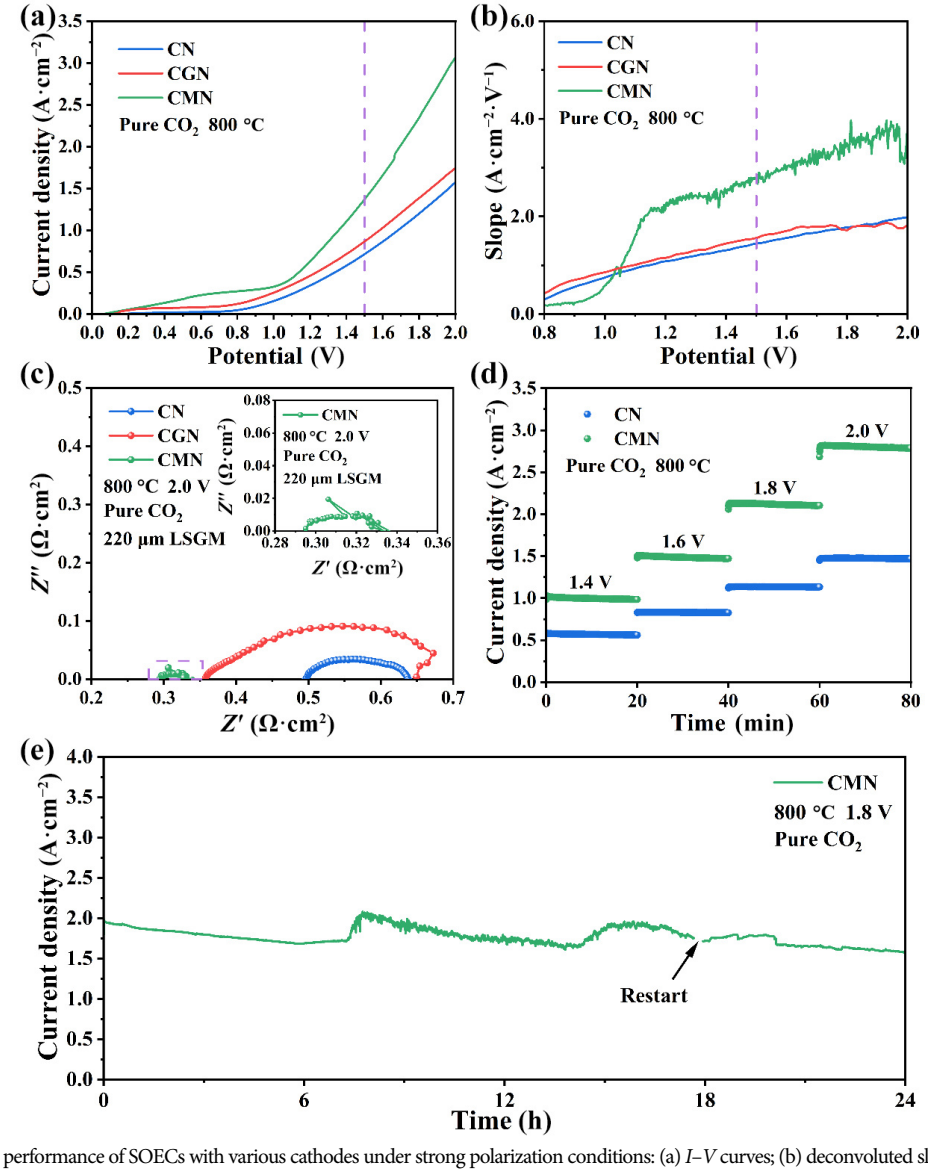

Fig. 6 Electrochemical performance of SOECs with various cathodes under strong polarization conditions: (a) *I–V* curves; (b) deconvoluted slope of *I–V* curves; (c) EIS results at 2.0 V; (d) short-term current stability; (e) long-term current stability.

ohmic and polarization resistances. To avoid electrolyte breakdown under high applied voltages, the electrolyte thickness was increased from 150 to 220 μm under these conditions, which consequently resulted in a higher ohmic resistance among the tested samples, whereas CGN showed the highest polarization resistance (Fig. 6(c)). This disparity highlights the distinct functionalities of the dopant Mn as a multivalent transition metal that promotes the formation of oxygen vacancies/Ce^{3+} through charge compensation upon substitution for Ce^{4+} and participates in redox reactions during electrolysis, thereby enhancing both the electronic conductivity and ionic conductivity [59]. Its synergistic interaction with exsolved Ni particles effectively accelerates CO_2 surface reaction kinetics and reduces polarization losses. In contrast, Gd, although capable of improving ionic conductivity, lacks redox activity and has low electronic conductivity. As a result, the Gd-doped electrodes exhibit fewer active sites for CO_2 adsorption/activation and higher series and electrode reaction polarization resistance than their Mn/Ni-codeped counterparts.

Short-term stability tests at 1.8 and 2.0 V (Fig. 6(d)) demonstrated that both the CN and CMN cathodes maintained stable current outputs without significant degradation, confirming their suitability for high-voltage CO_2 electroreduction. This is significantly different from those of perovskite oxide-based cathodes, where obvious degradation is observed with increased cell operating voltage [36,58], shedding light on the robust lattice stability of the ceria-based cathode. During the 24-h stability test at 800 °C and 1.8 V in pure CO_2, the cell with the CMN cathode exhibits a moderate current decay rate of ~17 $mA{\cdot}cm^{-2}{\cdot}h^{-1}$, indicative of a gradual increase in resistance (Fig. 6(e)). In the first 20 h, however, notable current fluctuations are observed: After an initial decline within the first 6 h, a sudden current surge occurs at approximately 6–8 h, which can be attributed to voltage-driven activation of the CMN cathode via enhanced $Ce^{4+} \rightarrow Ce^{3+}$ reduction, oxygen-vacancy formation, and Ni exsolution, leading to improved conductivity and CO_2 activation. Subsequent small oscillations superimposed on the slow decay likely arise from dynamic surface processes, such as transient carbonate adsorption/desorption and local redox cycling at the Ni–ceria interface. The brief recovery after the restart further supports the role of surface reorganization and removal of the inhibiting species. Overall, the current response reflects a balance between voltage-induced activation and gradual microstructural or surface state evolution. The signal peaks corresponding to carbonate species and carbon deposition were not detected in the post-tested Raman spectra, indicating the acceptable carbon tolerance of the CMN cathode under strong polarization conditions (Figure S24(a) in the ESM). Compared with the pre-test cell (Fig. S7 in the ESM), there was no clear evolution in the microstructure of the electrodes after the strong polarization long-term test (Figs. S24(b)–S24(f) in the ESM), indicating that the structure of the electrodes can remain stable at such a high applied voltage.

In previous studies on CeO_2-based cathodes for CO_2 reduction in SOECs, the improved electrochemical performance was generally attributed to the enhanced activity of exsolved metal particles or the metal/ceria interface, whereas little attention has been given to the bulk properties of the ceria matrix. Although classically doped ceria is a mixed ionic and electronic conductor, it is generally recognized that ionic conductivity is the major contributor, as Sm- or Gd-doped ceria have previously been considered potential options for electrolyte materials. For the SOEC electrode, the electrochemical reaction takes place at the triple phase boundary, where the ionic conductor, electronic conductor, and CO_2 meet. In our study, the limited electronic conductivity of the ceria-based electrode unexpectedly increases the series resistance (Figs. 5(b) and 6(c), Figs. S12–S16 and S21–S23 in the ESM). Moreover, according to Kamboj *et al.* [38] and Badwal *et al.* [60], Ce^{3+} serves as the active site for the CO_2RR and is considered highly related to the electronic conductivity of the ceria material. Maximizing the Ce^{3+} content in the cathodic ceria electrocatalyst is expected to further improve the catalytic activity of the CO_2RR. In this work, both the doping of Mn cations and the application of high voltage or strong polarization conditions improved the Ce^{3+} content in the bulk material. When further combined with the redox Mn cation effect and the well-built nanoscale Ni-ceria heterostructure, the bulk and surface comodified ceria cathodic catalysts demonstrated exceptional catalytic activity for CO_2 reduction under strong polarization condition, which was accompanied by the expected durability because of the redox-stable ceria-based matrix in the SOEC cathode.

The doped and structurally modified ceria-based cathode materials demonstrate remarkable CO_2 electroreduction performance under both conventional and high-voltage operating conditions. Under strong polarization conditions (1.8 V), these materials sustain high current densities with slight degradation, indicating acceptable electrochemical robustness and catalytic efficiency. The codoping of multivalent transition metals such as Mn and Ni significantly enhances oxygen vacancy formation, facilitates electron and ion transport, and accelerates surface reaction kinetics. Owing to the promoted ceria reduction under strong polarization conditions, these combined effects not only reduce the polarization resistance but also expand the density of active sites for CO_2 activation. The results highlight the effectiveness of tailored doping and practical operational strategies for optimizing the functional properties of ceria-based cathodes, offering a viable pathway toward high-efficiency and durable CO_2 electroreduction under industrially relevant conditions.

4 Conclusions

In this study, a series of ceria-based cathode materials was developed and systematically investigated for high-temperature CO_2 electroreduction in SOECs. The Mn, Ni codoping strategy not only facilitates the formation of active surface Ni–ceria heterostructures but also increases the Ce^{3+} concentration and number of oxygen defects in the bulk lattice. These factors increase the number of electrochemically active sites for CO_2 adsorption and activation as well as the electrical conductivities of the electrodes (ions and electrons). Thus, the catalytic activity of the ceria-based cathode is promoted through multiple pathways. Bulk Ce^{3+} phase enrichment, redox Mn cations, and surface-coupled Ni–Ce active sites synergistically enhance CO_2 adsorption–activation behavior, i.e., reaction kinetics, and charge transport in the SOEC electrode. Under mild electrolysis conditions, the optimized CMN cathode exhibited reliable electrochemical performance for nearly 140 h at 750 °C and 1.1 V without carbon deposition, matrix phase and microstructural change. Furthermore, under strong polarization conditions (2.0 V), the CMN cathode delivered a high current density of 3.05 $A{\cdot}cm^{-2}$ at 800 °C and sustained stable high-current electroreduction for 24 h at 1.8 V, underscoring its robust structural and electrochemical stability for practical CO_2RR applications. In the future, research may emphasize deepening the understanding of defect–metal interactions at the atomic scale, refining the redox dynamics during electrolysis, and developing hierarchical electrode architectures that simultaneously optimize active site accessibility and gas diffusion pathways, thereby unlocking greater catalytic

efficiency and stability of ceria-based cathode catalysts for next-generation SOEC systems. Overall, this work provides valuable insights into the rational design of advanced ceria-based cathodes for durable and efficient high-temperature CO_2 electroreduction under both moderately and strongly polarized conditions, potentially increasing the technical readiness of SOEC technology.

Acknowledgements

This work was financially supported by the National Natural Science Foundation of China (No. 22378268), the Guangdong Basic and Applied Basic Research Foundation (No. 2024A1515012212), and the Shenzhen University-National Taipei University of Technology Joint Research Program (Nos. 2026008 and 2023011). The authors also acknowledge the Instrumental Analysis Center of Shenzhen University (Xili Campus), the Electron Microscopy Centre of Shenzhen University.

Author contributions

Yongjian Chen: methodology, investigation, formal analysis, writing—original draft, and writing—review & editing; Ciyuan Deng, Wanying Luo, Hongming Ye, and Rui Yang: investigation, formal analysis, and validation; Manish Singh: writing—review & editing; Te-Wei Chiu: supervision and writing—review & editing; Liangdong Fan: conceptualization, methodology, resources, writing—original draft, writing—review & editing, supervision, and funding acquisition. All the authors discussed the results and commented on the manuscript.

Availability of data and materials

The data that support the findings of this study are available from the corresponding author upon reasonable request.

Competing interests

The authors have no competing interests that are relevant to the content of this article.

Electronic Supplementary Material

Supplementary material is available in the online version of this article at https://doi.org/10.26599/JAC.2025.9221219.

References

[1] Jang I, Carneiro JSA, Crawford JO, *et al.* Electrocatalysis in solid oxide fuel cells and electrolyzers. *Chem Rev* 2024, **124**: 8233–8306.

[2] Monteiro MCO, Philips MF, Schouten KJP, *et al.* Efficiency and selectivity of CO_2 reduction to CO on gold gas diffusion electrodes in acidic media. *Nat Commun* 2021, **12**: 4943.

[3] Xing Z, Hu L, Ripatti DS, *et al.* Enhancing carbon dioxide gas-diffusion electrolysis by creating a hydrophobic catalyst microenvironment. *Nat Commun* 2021, **12**: 136.

[4] Sun Q, Jia C, Lu HC, *et al.* Ampere-level electroreduction of CO_2 and CO. *Chem Soc Rev* 2025, **54**: 6973–7016.

[5] Kim C, Bui JC, Luo XY, *et al.* Tailored catalyst microenvironments for CO_2 electroreduction to multicarbon products on copper using bilayer ionomer coatings. *Nat Energy* 2021, **6**: 1026–1034.

[6] Gu JM, Kim H, Zhao JZ, *et al.* Anchored PtSn nanoalloys via *in situ* exsolution for enhanced solid oxide cell performance. *Rare Metals* 2025, **44**: 7846–7858.

[7] Chen W, Sun CW. Recent advances in high temperature solid oxide electrolytic cells. *Energy Mater* 2025, **5**: 500045.

[8] Zhang MY, Tian YF, Zou L, *et al.* Synergistic enhancement of electrochemical performance in reversible solid oxide cells via deficiency-induced oxygen vacancy and nanoparticle generation. *Rare Metals* 2025, **44**: 264–274.

[9] Ren QH, Zhang Y, Tao HL, *et al.* An innovative and facile synthesis route of $(La,Sr)_2FeO_{4+\delta}$–$La_{0.4}Sr_{0.6}FeO_{3-\delta}$ composite as a highly stable air electrode for reversible solid oxide cell applications. *J Adv Ceram* 2024, **13**: 1337–1348.

[10] Nielsen DU, Hu XM, Daasbjerg K, *et al.* Chemically and electrochemically catalysed conversion of CO_2 to CO with follow-up utilization to value-added chemicals. *Nat Catal* 2018, **1**: 244–254.

[11] Zheng YF, Yang H, Pan ZH, *et al.* A Ca and Fe Co-doped layered perovskite as stable air electrode in solid oxide electrolyzer cells under high-current electrolysis. *Electrochim Acta* 2017, **251**: 581–587.

[12] Lv XM, Chen MH, Xie ZL, *et al.* Electrochemical conversion of C1 molecules to sustainable fuels in solid oxide electrolysis cells. *Chinese J Catal* 2022, **43**: 92–103.

[13] Fan LD, Luo WY, Fan QX, *et al.* Status and outlook of solid electrolyte membrane reactors for energy, chemical, and environmental applications. *Chem Sci* 2025, **16**: 6620–6687.

[14] Zhang N, Zhang WY, Gong YS, *et al.* Enhanced stability of perovskite cathode via entropy engineering for CO_2 electrolysis. *Rare Metals* 2025, **44**: 2416–2427.

[15] Qiu P, Li C, Liu B, *et al.* Materials of solid oxide electrolysis cells for H_2O and CO_2 electrolysis: A review. *J Adv Ceram* 2023, **12**: 1463–1510.

[16] Lin WB, Su WB, Li YP, *et al.* Enhancing electrochemical CO_2 reduction on perovskite oxide for solid oxide electrolysis cells through *in situ* A-site deficiencies and surface carbonate deposition induced by lithium cation doping and exsolution. *Small* 2023, **19**: 2303305.

[17] Yang XX, Sun KN, Ma MJ, *et al.* Achieving strong chemical adsorption ability for efficient carbon dioxide electrolysis. *Appl Catal B—Environ* 2020, **272**: 118968.

[18] Tan T, Wang ZM, Qin MX, *et al. In situ* exsolution of core–shell structured NiFe/FeO_x nanoparticles on $Pr_{0.4}Sr_{1.6}(NiFe)_{1.5}Mo_{0.5}O_{6-\delta}$ for CO_2 electrolysis. *Adv Funct Mater* 2022, **32**: 2202878.

[19] Li ZS, Peng ML, Zhu YL, *et al.* The facilitated cathodic elementary reactions of solid oxide electrolysis cells for CO_2 conversion over a Ce decorated $La_{0.43}Ca_{0.37}Ti_{0.94}Ni_{0.06}O_{3-\delta}$ electrocatalyst. *J Mater Chem A* 2022, **10**: 20350–20364.

[20] Shang YJ, Smitshuysen AL, Yu M, *et al.* 3D microstructural characterization of Ni/yttria-stabilized zirconia electrodes during long-term CO_2 electrolysis. *J Mater Chem A* 2023, **11**: 12245–12257.

[21] Hu SQ, Pang BJ, Zhang LM, *et al.* Mapping a thermodynamic stability window to prevent detrimental reactions during CO_2 electrolysis in solid oxide electrolysis cells. *Appl Catal B—Environ* 2023, **324**: 122239.

[22] Yue WX, Li YF, Zheng Y, *et al.* Enhancing coking resistance of Ni/YSZ electrodes: *In situ* characterization, mechanism research, and surface engineering. *Nano Energy* 2019, **62**: 64–78.

[23] Hubert M, Laurencin J, Cloetens P, *et al.* Impact of Nickel agglomeration on Solid Oxide Cell operated in fuel cell and electrolysis modes. *J Power Sources* 2018, **397**: 240–251.

[24] Zhang LH, Sun W, Xu CM, *et al.* Two-fold improvement in chemical adsorption ability to achieve effective carbon dioxide electrolysis. *Appl Catal B—Environ* 2022, **317**: 121754.

[25] Lv HF, Lin L, Zhang XM, *et al.* Promoting exsolution of RuFe alloy nanoparticles on $Sr_2Fe_{1.4}Ru_{0.1}Mo_{0.5}O_{6-\delta}$ via repeated redox manipulations for CO_2 electrolysis. *Nat Commun* 2021, **12**: 5665.

[26] Yang R, Lin WB, He YJ, *et al.* Revealing the detrimental CO_2 reduction effect of $La_{0.6}Sr_{0.4}FeO_{3-\delta}$-derived heterostructure in solid oxide electrolysis cells. *iScience* 2024, **27**: 109648.

[27] Liu DL, Shang H, Zhou C, *et al.* Active Cu and Fe nanoparticles codecorated ruddlesden–popper-type perovskite as solid oxide electrolysis cells cathode for CO_2 splitting. *Energy Environ Mater* 2024, **7**: 12717.

[28] Wang WH, Li HX, Park KY, *et al.* Enhancing direct eectrochemical CO_2 electrolysis by introducing A-site deficiency for dual-phase Pr(Ca)Fe(Ni)$O_{3-\delta}$ cathode. *Energy Environ Mater* 2024, **7**: 12715.

[29] Zhang BW, Zhu MN, Gao MR, *et al.* Boosting the stability of perovskites with exsolved nanoparticles by B-site supplement mechanism. *Nat Commun* 2022, **13**: 4618.
[30] Lee S, Kim M, Lee KT, *et al.* Enhancing electrochemical CO_2 reduction using Ce(Mn,Fe)O_2 with La(Sr)Cr(Mn)O_3 cathode for high-temperature solid oxide electrolysis cells. *Adv Energy Mater* 2021, **11**: 2100339.
[31] Li YH, Li Y, Wan YH, *et al.* Perovskite oxyfluoride electrode enabling direct electrolyzing carbon dioxide with excellent electrochemical performances. *Adv Energy Mater* 2019, **9**: 1803156.
[32] Yang CC, Wang YH, Tian YF, *et al.* Electrochemical performance of symmetric solid oxide cells employing a Sc-doped $SrFeO_{3-\delta}$-based electrode. *Chem Eng J* 2024, **485**: 149970.
[33] Zhang NX, Naden A, Zhang LH, *et al.* Enhanced CO_2 electrolysis through Mn substitution coupled with Ni exsolution in lanthanum calcium titanate electrodes. *Chem Eng J* 2024, **36**: e2308481.
[34] Lee SW, Nam TH, Lee SH, *et al.* Ultrasonic spraying of Ce(Mn,Fe)O_2 nanocatalysts onto a perovskite surface for highly efficient electrochemical CO_2 reduction. *Energ Environ Sci* 2025, **18**: 1205–1213.
[35] Shen YX, Wang S, Li RT, *et al. In situ* self-assembled active and stable Ir@MnO_x/$La_{0.7}Sr_{0.3}Cr_{0.9}Ir_{0.1}O_{3-\delta}$ interfaces for CO_2 electrolysis. *Angew Chem Int Edit* 2024, **63**: 202404861.
[36] Li YH, Singh M, Zhuang ZC, *et al.* Efficient reversible CO/CO_2 conversion in solid oxide cells with a phase-transformed fuel electrode. *Sci China Mater* 2021, **64**: 1114–1126.
[37] Thalinger R, Gocyla M, Heggen M, *et al.* Exsolution of Fe and SrO nanorods and nanoparticles from lanthanum strontium ferrite $La_{0.6}Sr_{0.4}FeO_{3-\delta}$ materials by hydrogen reduction. *J Phys Chem C* 2015, **119**: 22050–22056.
[38] Kamboj V, Raychowdhury S, Ranjan C. Operando studies on solid oxide ceria electrodes during CO_2 electroreduction. *Appl Catal B—Environ* 2025, **365**: 124880.
[39] Zhang LJ, Jiang YN, Zhu K, *et al.* Fe-doped ceria-based ceramic cathode for high-efficiency CO_2 electrolysis in solid oxide electrolysis cell. *Small Methods* 2024, **8**: 2301686.
[40] Jiang YN, Ye LJ, Zhang SW, *et al.* Doped ceria with exsolved Fe0 nanoparticles as a Sr-free cathode for CO_2 electrolysis in SOECs at reduced temperatures. *J Mater Chem A* 2022, **10**: 9380–9383.
[41] Li M, Hua B, Wang LC, *et al.* Switching of metal–oxygen hybridization for selective CO_2 electrohydrogenation under mild temperature and pressure. *Nat Catal* 2021, **4**: 274–283.
[42] Elias JS, Risch M, Giordano L, *et al.* Structure, bonding, and catalytic activity of monodisperse, transition-metal-substituted CeO_2 nanoparticles. *J Am Chem Soc* 2014, **136**: 17193–17200.
[43] Zheng Y, Chen ZW, Zhang JJ. Solid oxide electrolysis of H_2O and CO_2 to produce hydrogen and low-carbon fuels. *Electrochem Energy R* 2021, **4**: 508–517.
[44] Ma WC, Morales-Vidal J, Tian JM, *et al.* Encapsulated Co–Ni alloy boosts high-temperature CO_2 electroreduction. *Nature* 2025, **641**: 1156–1161.
[45] Li YB, Ye LT, Xie K. Exsolution of Ni nanoparticles at the ceria electrode for boosting CO_2 electrolysis. *Int J Hydrogen Energ* 2025, **128**: 589–596.
[46] Huang ZD, Zhao Z, Qi HY, *et al.* Enhancing cathode performance for CO_2 electrolysis with $Ce_{0.9}M_{0.1}O_{2-\delta}$ (M = Fe, Co, Ni) catalysts in solid oxide electrolysis cell. *J Energy Chem* 2020, **40**: 46–51.
[47] Uecker J, Unachukwu ID, Vibhu V, *et al.* Gadolinium doped ceria as nickel-free fuel electrode in high temperature CO_2-electrolysis. *ChemElectroChem* 2024, **11**: 202300617.
[48] Zhou YJ, Wei FF, Wu HH. Fe-decorated on Sm-doped CeO_2 as cathodes for high-temperature CO_2 electrolysis in solid oxide electrolysis cells. *Electrochim Acta* 2022, **419**: 140434.
[49] Kamboj V, Raychowdhury S, Ranjan C. Diving deep into solid oxide-based CO_2 electrolysis: operando insights. *Curr Opin Electroche* 2024, **46**: 101514.
[50] Wu TT, Qin RM, Zhang JR, *et al.* Enhanced high-temperature CO_2 electrolysis on CeO_2 by inducing under-coordinated dual-atom active sites. *J Catal* 2024, **429**: 115251.
[51] Wan TH, Saccoccio M, Chen C, *et al.* Influence of the discretization methods on the distribution of relaxation times deconvolution: Implementing radial basis functions with DRTtools. *Electrochim Acta* 2015, **184**: 483–499.
[52] He F, Hou MY, Zhu F, *et al.* Building efficient and durable hetero-interfaces on a perovskite-based electrode for electrochemical CO_2 reduction. *Adv Energy Mater* 2022, **12**: 2202175.
[53] Zhang L, Zhang WK, Poh CK, *et al.* Catalytic decomposition of methane: Ni-promoted perovskite oxide catalysts for turquoise hydrogen and carbon nanomaterials co-production. *Energy Mater* 2025, **5**: 500023.
[54] Luo J, Ke YD, Li QY, *et al.* A novel symmetrical SOFC with thin BZCY electrolyte and PBFNCM-BZCY electrodes for electricity and ethylene co-production through ethane dehydrogenation. *Rare Metals* 2025, **44**: 6175–6184.
[55] Wang TB, Mao Y, Ou PF, *et al.* B-site-metal-mediated coke-resistant CO_2 electrolysis on perovskite surfaces. *Adv Sci* 2025, **12**: 03970.
[56] Hu XG, Liu LM, Zhou XL, *et al.* Electrochemical behaviors of copper /manganese-doped ceria cermet as a fuel electrode for high-temperature solid oxide cells. *J Appl Electrochem* 2023, **53**: 121–130.
[57] Zagaynov IV, Naumkin AV, Konovalov AA, *et al.* Catalytic activity of ceria-based solid solutions with low-content dopants. *Chem Eng J* 2024, **489**: 151340.
[58] Sagar VT, Pintar A. Enhanced surface properties of CeO_2 by MnO_x doping and their role in mechanism of methane dry reforming deduced by means of *in situ* DRIFTS. *Appl Catal A—Gen* 2020, **599**: 117603.
[59] Opitz AK, Nenning A, Vonk V, *et al.* Understanding electrochemical switchability of perovskite-type exsolution catalysts. *Nat Commun* 2020, **11**: 4801.
[60] Badwal SPS, Ciacchi FT, Drennan J. Investigation of the stability of ceria-gadolinia electrolytes in solid oxide fuel cell environments. *Solid State Ionics* 1999, **121**: 253–262.